Supplemental Materials

Contents

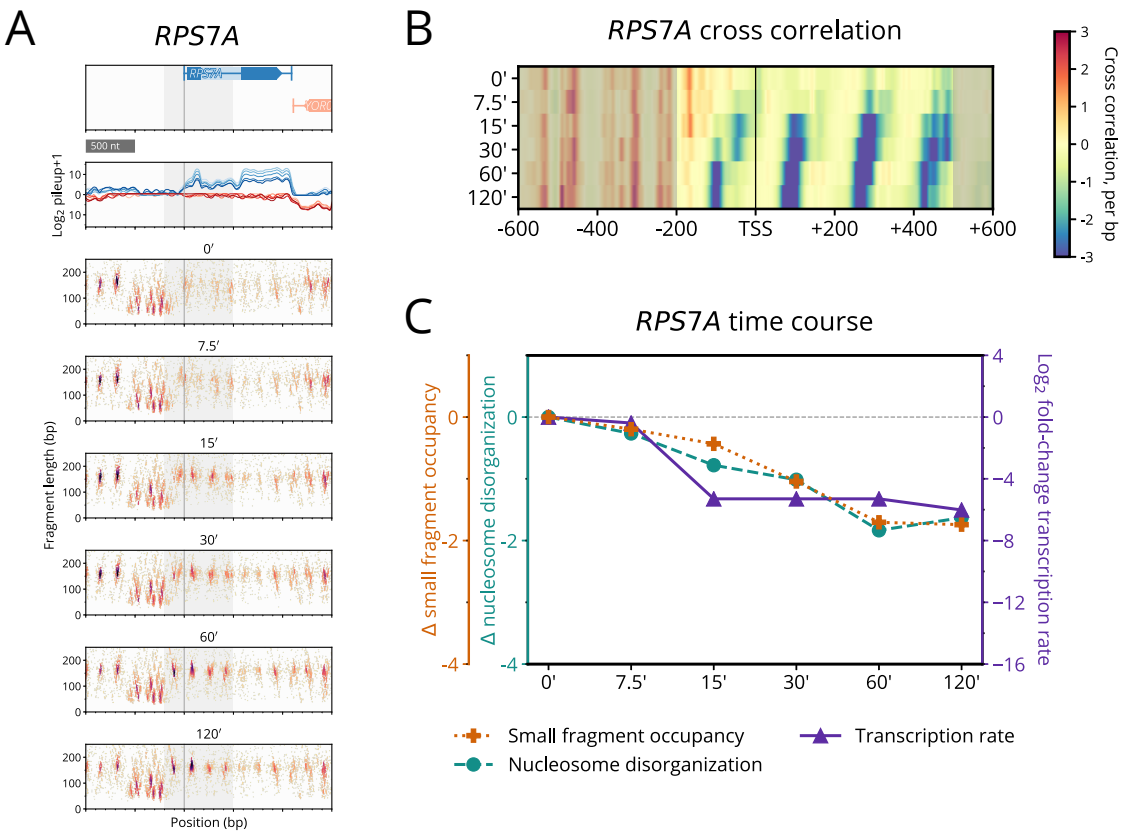

Supplemental Figure S1. Chromatin local to *RPS7A*, encoding a small ribosomal subunit protein, changes in accordance with its repression in transcription. **(A)** Typhoon plot shows that the nucleosomes in the gene body of *RPS7A* become well-organized over the 120 min time course. **(B)** Cross-correlation heatmap shows the upstream shift of the nucleosomes in the the gene body of *RPS7A*, as well as a replacement of small fragments with nucleosome-sized fragments 200 bp upstream of its TSS. **(C)** Line plot shows that both reduced promoter occupancy and an organization of gene body nucleosomes coincide with decreased transcription of *RPS7A*.

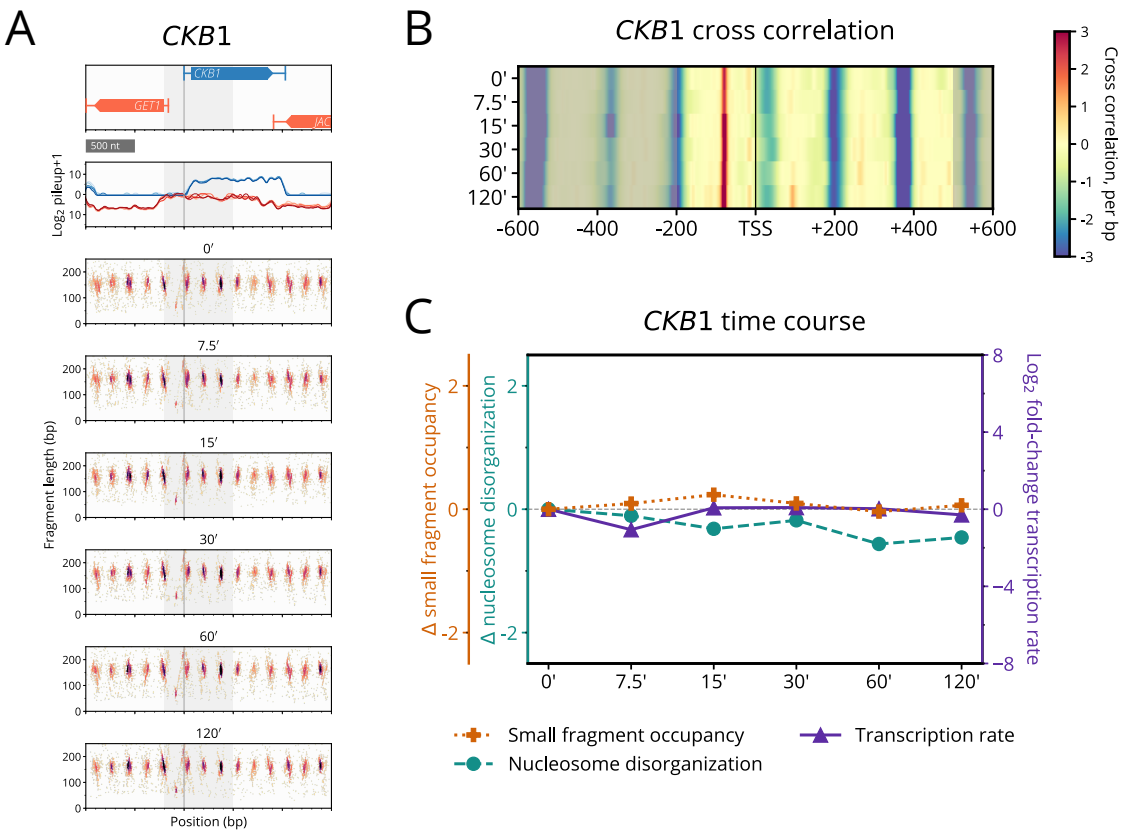

Supplemental Figure S2. *CKB1*, coding for a cell growth protein kinase, exhibits unchanging transcript levels and chromatin. **(A)** Typhoon plot of *CKB1* shows transcription and chromatin do not change over the duration of the 120 min time course. **(B)** Cross-correlation heatmap shows the chromatin local to the TSS of *CKB1* is essentially constant. **(C)** Line plot showing the nearly unchanging promoter occupancy, nucleosome disorganization, and transcription of *CKB1* through 120 min.

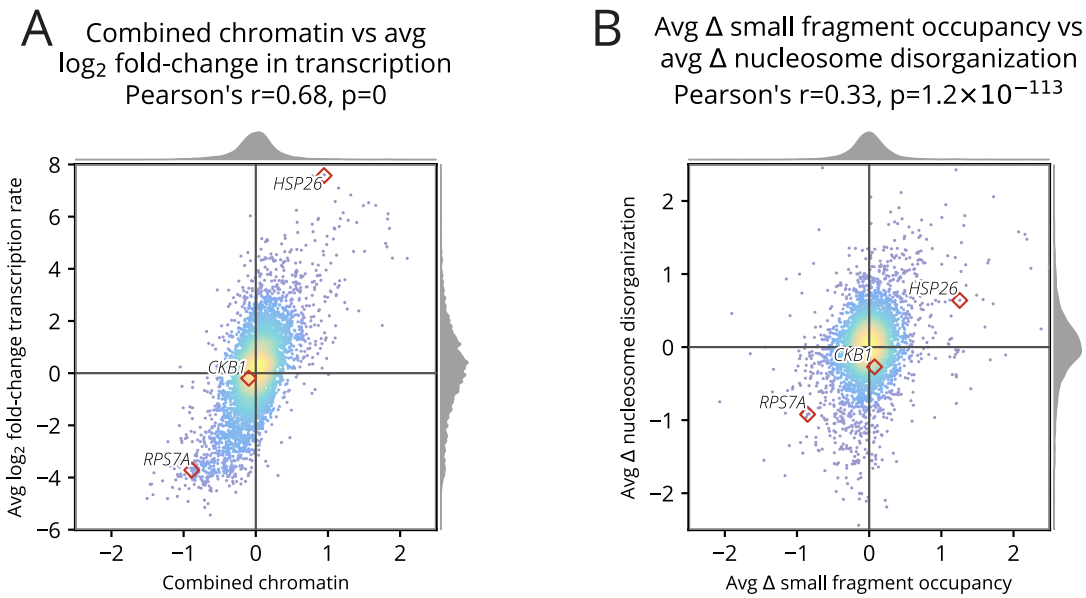

Supplemental Figure S3. Changes in orthogonal chromatin measures are correlated with $\log_2$ fold-changes in transcription. **(A)** Scatter plot shows our combined chromatin score is correlated with average $\log_2$ fold-change in transcription with r=0.68. **(B)** Scatter plot shows average change in small fragment occupancy and average change in nucleosome disorganization are less correlated, with r=0.33, indicative of the orthogonal statistical power of each in correlating with changes in transcription.

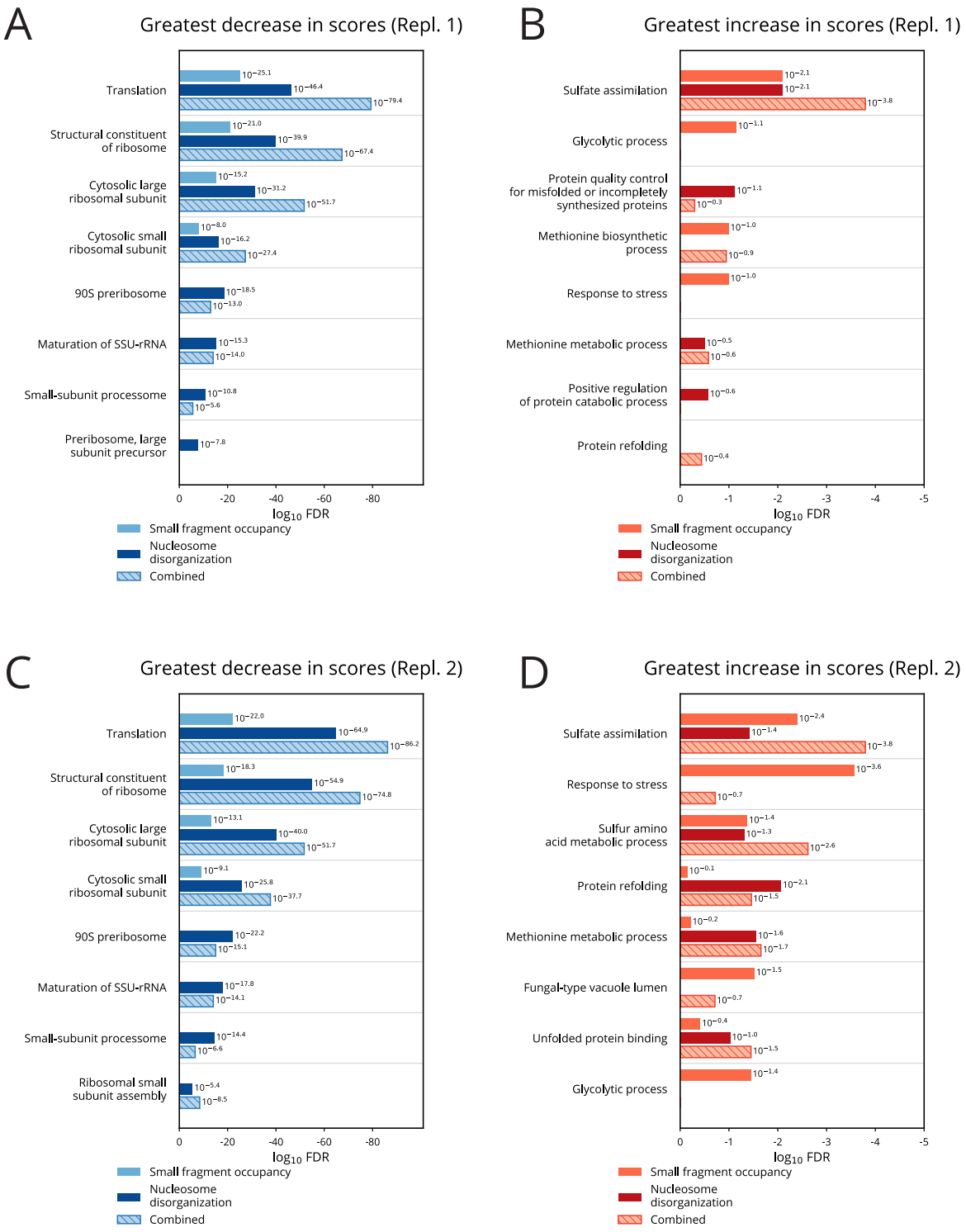
A
Greatest decrease in scores (Repl. 1)
Translation
Structural constituent of ribosome
Cytosolic large ribosomal subunit
Cytosolic small ribosomal subunit
90S preribosome
Maturation of SSU-rRNA
Small-subunit processome
Preribosome, large subunit precursor
$10^{-25.1}$
$10^{-46.4}$
$10^{-79.4}$
$10^{-21.0}$
$10^{-39.9}$
$10^{-67.4}$
$10^{-15.2}$
$10^{-31.2}$
$10^{-51.7}$
$10^{-8.0}$
$10^{-16.2}$
$10^{-27.4}$
$10^{-18.5}$
$10^{-13.0}$
$10^{-15.3}$
$10^{-14.0}$
$10^{-10.8}$
$10^{-5.6}$
$10^{-7.8}$
0
-20
-40
-60
-80
$\log_{10}$ FDR
Small fragment occupancy
Nucleosome disorganization
Combined
B
Greatest increase in scores (Repl. 1)
Sulfate assimilation
Glycolytic process
Protein quality control for misfolded or incompletely synthesized proteins
Methionine biosynthetic process
Response to stress
Methionine metabolic process
Positive regulation of protein catabolic process
Protein refolding
$10^{-2.1}$
$10^{-2.1}$
$10^{-3.8}$
$10^{-1.1}$
$10^{-1.1}$
$10^{-0.3}$
$10^{-1.0}$
$10^{-0.9}$
$10^{-1.0}$
$10^{-0.5}$
$10^{-0.6}$
$10^{-0.6}$
$10^{-0.4}$
0
-1
-2
-3
-4
-5
$\log_{10}$ FDR
Small fragment occupancy
Nucleosome disorganization
Combined
C
Greatest decrease in scores (Repl. 2)
Translation
Structural constituent of ribosome
Cytosolic large ribosomal subunit
Cytosolic small ribosomal subunit
90S preribosome
Maturation of SSU-rRNA
Small-subunit processome
Ribosomal small subunit assembly
$10^{-22.0}$
$10^{-64.9}$
$10^{-86.2}$
$10^{-18.3}$
$10^{-54.9}$
$10^{-74.8}$
$10^{-13.1}$
$10^{-40.0}$
$10^{-51.7}$
$10^{-9.1}$
$10^{-25.8}$
$10^{-37.7}$
$10^{-22.2}$
$10^{-15.1}$
$10^{-17.8}$
$10^{-14.1}$
$10^{-14.4}$
$10^{-6.6}$
$10^{-5.4}$
$10^{-8.5}$
0
-20
-40
-60
-80
$\log_{10}$ FDR
Small fragment occupancy
Nucleosome disorganization
Combined
D
Greatest increase in scores (Repl. 2)
Sulfate assimilation
Response to stress
Sulfur amino acid metabolic process
Protein refolding
Methionine metabolic process
Fungal-type vacuole lumen
Unfolded protein binding
Glycolytic process
$10^{-2.4}$
$10^{-1.4}$
$10^{-3.8}$
$10^{-3.6}$
$10^{-0.7}$
$10^{-1.4}$
$10^{-1.3}$
$10^{-2.6}$
$10^{-0.1}$
$10^{-2.1}$
$10^{-1.5}$
$10^{-0.2}$
$10^{-1.6}$
$10^{-1.7}$
$10^{-1.5}$
$10^{-0.7}$
$10^{-0.4}$
$10^{-1.0}$
$10^{-1.5}$
$10^{-1.4}$
0
-1
-2
-3
-4
-5
$\log_{10}$ FDR
Small fragment occupancy
Nucleosome disorganization
Combined

Supplemental Figure S4. **(A, B)** Gene Ontology (GO) categories with the most significant enrichment among the 300 genes showing the greatest decrease (A) and increase (B) in various chromatin scores in replicate 1. **(C, D)** GO categories with the most significant enrichment among the 300 genes showing the greatest decrease (C) and increase (D) in various chromatin scores in replicate 2. In each case, the 8 most significant GO categories are shown, as in the paper. Both replicates recover down-regulated translation and multiple ribosomal subunit pathways with similar significance, and both replicates recover up-regulated sulfate assimilation and glycolytic process pathways with similar significance. Replicate 2 recovers up-regulated stress response, methionine metabolism, and protein refolding pathways with slightly greater significance than replicate 1 does, though all of these GO categories still appear in the top 8 of both.

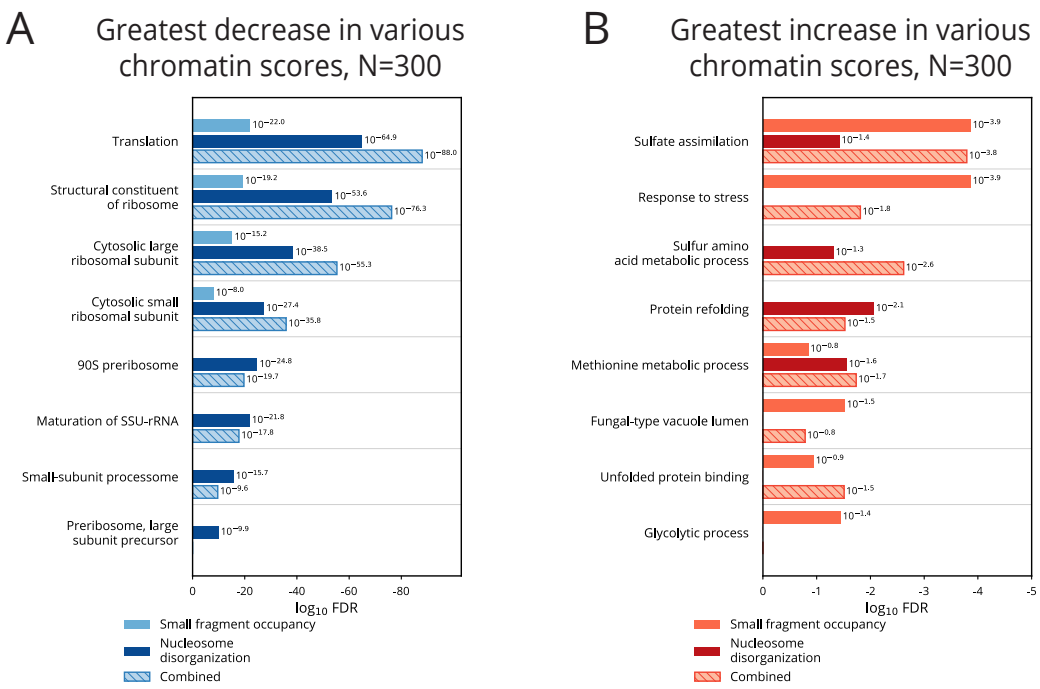

Supplemental Figure S5. GO enrichment analysis of genes with highly dynamic chromatin recovers established cadmium response pathways. **(A)** Top 8 categories resulting from GO enrichment analysis of 300 genes with greatest decrease in small fragment occupancy, nucleosome disorganization, and combined chromatin score. Translation-related genes are recovered with significant FDR. **(B)** Top 8 categories resulting from GO enrichment analysis of 300 genes with greatest increase in small fragment occupancy, nucleosome disorganization, and combined chromatin score. Genes involved with stress response, sulfur assimilation, and protein folding pathways are recovered with significant FDR.

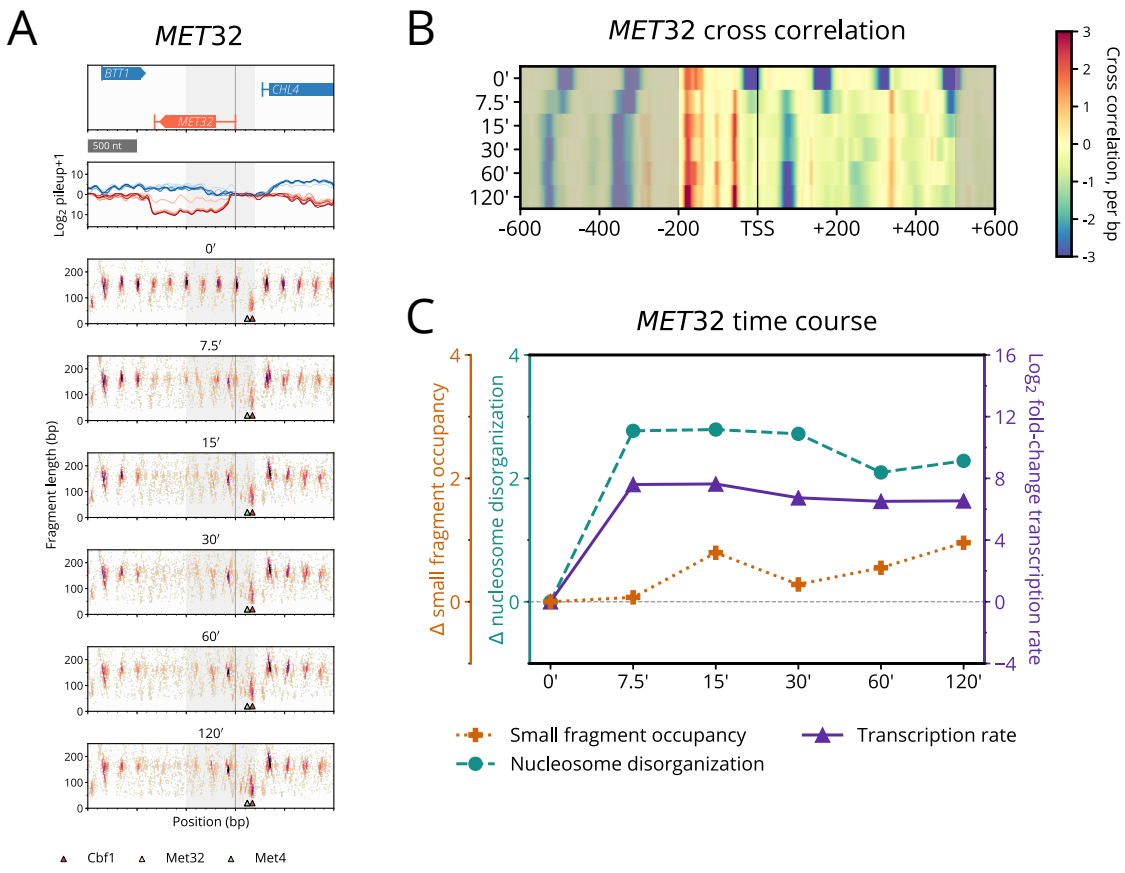

Supplemental Figure S6. Sulfur pathway gene *MET32* activates with binding dynamics local to Met4 complex binding. **(A)** *MET32* typhoon plot shows changes in small fragments at motifs for TFs in the Met4 complex. Small fragments at a Cbf1 motif (red triangle) change from a clear well-positioned cluster at 0 min to an enrichment of small fragments near a Met4 motif (green triangle) and a Met32 motif (obscured by green triangle) from 7.5 min onward. **(B)** Cross-correlation heatmap of the dramatic chromatin changes at *MET32* beginning at 7.5 min. Changes include nucleosome disorganization, downstream shift of the +1 nucleosome, and increased occupancy of small fragments upstream of *MET32*. **(C)** Line plot shows the transcriptional activation of *MET32* at 7.5 min alongside significant nucleosome disorganization.

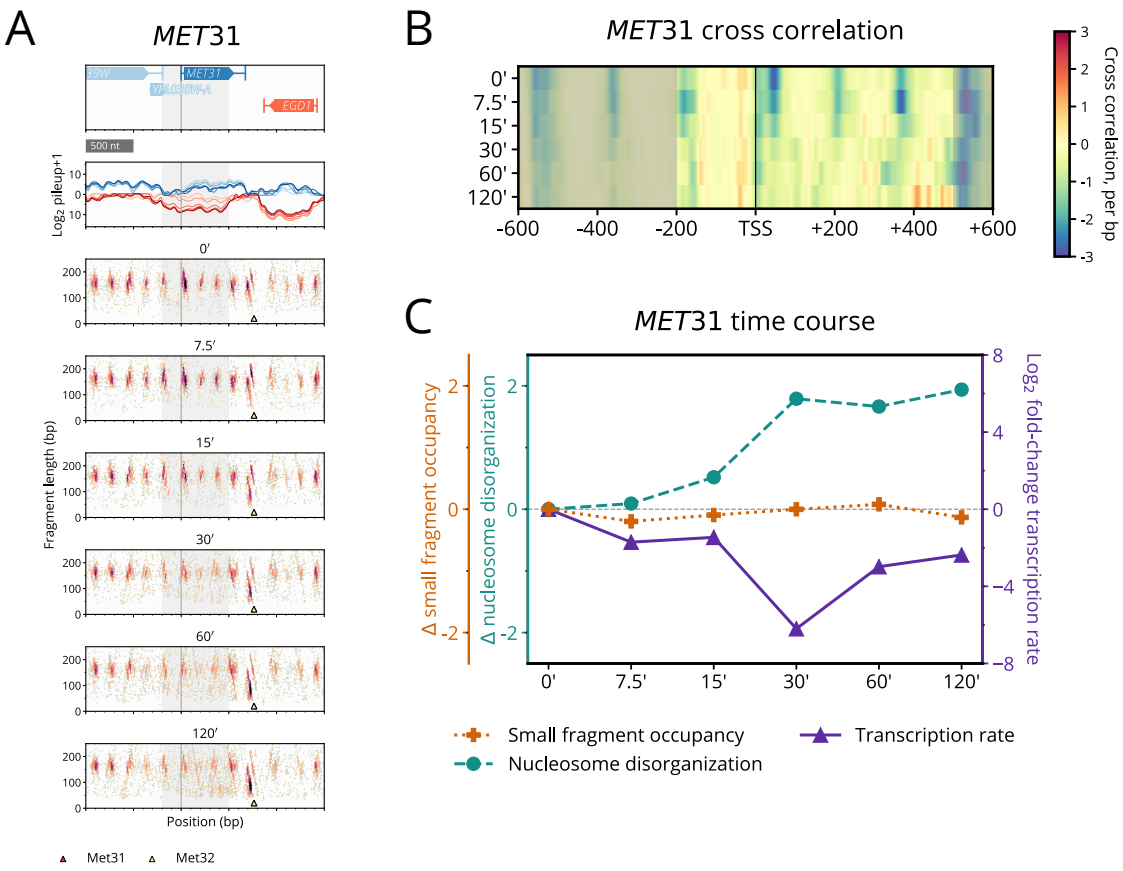

Supplemental Figure S7. Sense transcription of *MET31* is repressed while antisense transcription is induced. **(A)** Typhoon plot of *MET31* shows activation of antisense transcription within the transcript boundary of *MET31*, downstream of small fragment enrichment at a Met31/Met32 binding motif (yellow triangle). **(B)** Cross-correlation heatmap of *MET31* shows the nucleosome disorganization associated with an induction of antisense transcription. **(C)** Line plot shows the nucleosome disorganization of *MET31* is anti-correlated with its repressed sense transcription.

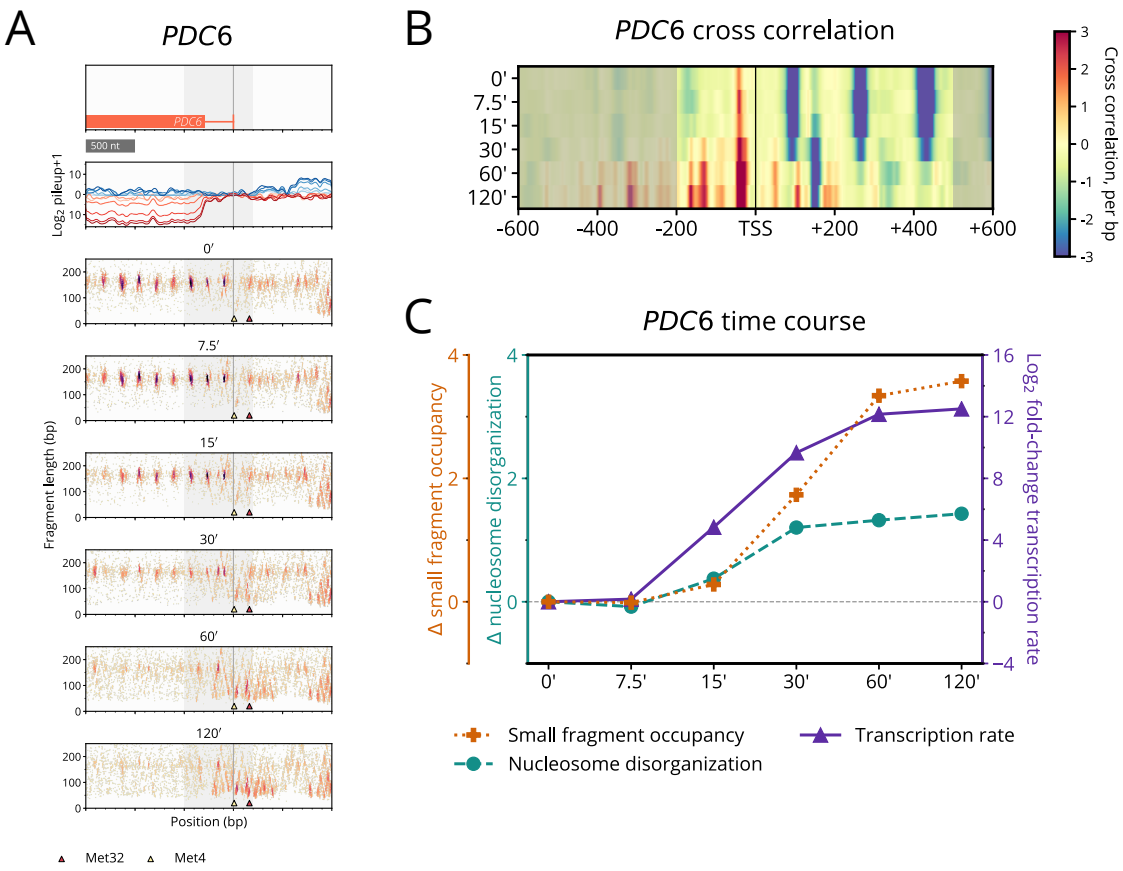

Supplemental Figure S8. Sulfur-saving *PDC6* is highly activated with dramatic changes in its local chromatin. **(A)** Typhoon plot of *PDC6* shows significant enrichment of small fragments at binding motifs for Met32 (red triangle) and Met4 (yellow triangle) beginning at 30 min. **(B)** Cross-correlation heatmap of *PDC6* shows a clear downstream shift of the +1 nucleosome and dramatic disorganization of other nucleosomes in the gene body between 30–120 min. **(C)** Line plot shows the highly activated transcription of *PDC6* is associated with significant enrichment of small fragments in the promoter and nucleosome disorganization in the gene body.

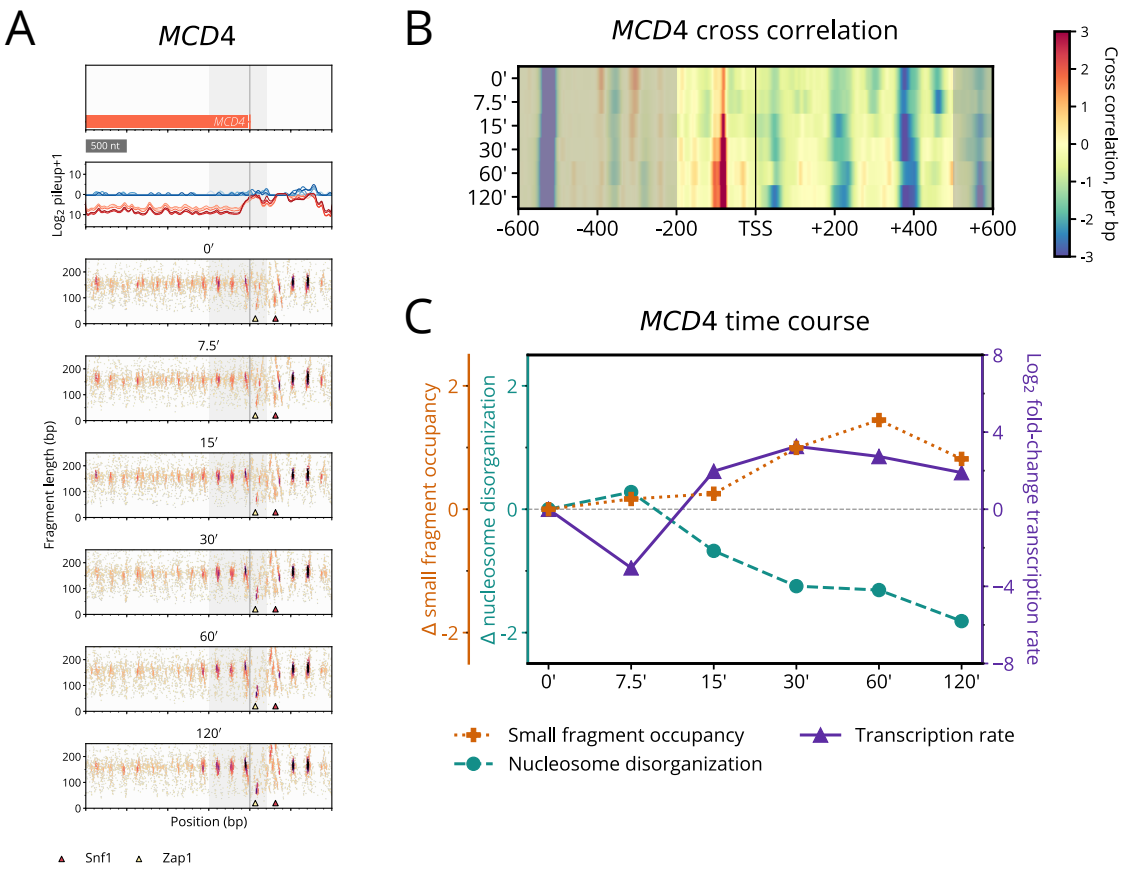

Supplemental Figure S9. The expression of *MCD4*, encoding an endoplasmic reticulum membrane protein, is up-regulated with evidence for changes in binding by known regulators Zap1 and Snf1 (Lyons *et al.* 2000; Venters *et al.* 2011), but also exhibits surprisingly increased nucleosome organization within its gene body. **(A)** Typhoon plot depicts the complex chromatin and transcription dynamics of *MCD4*. Along with increased transcription within the gene body of *MCD4*, a small transcript 200–300 bp upstream of the TSS is decreasing concomitantly. Time course shows monotonically changing binding at TF motifs flanking this upstream transcript. Small fragments become enriched at a Zap1 motif (yellow triangle). Small fragments at a Snf1 motif (red triangle) are replaced by fragments greater than 190 bp. **(B)** Cross-correlation heatmap depicts an enrichment of small fragments just upstream of *MCD4* as well as increased nucleosome organization. **(C)** Line plot shows an anti-correlated relationship between the decreased nucleosome disorganization and increased transcription of *MCD4*.

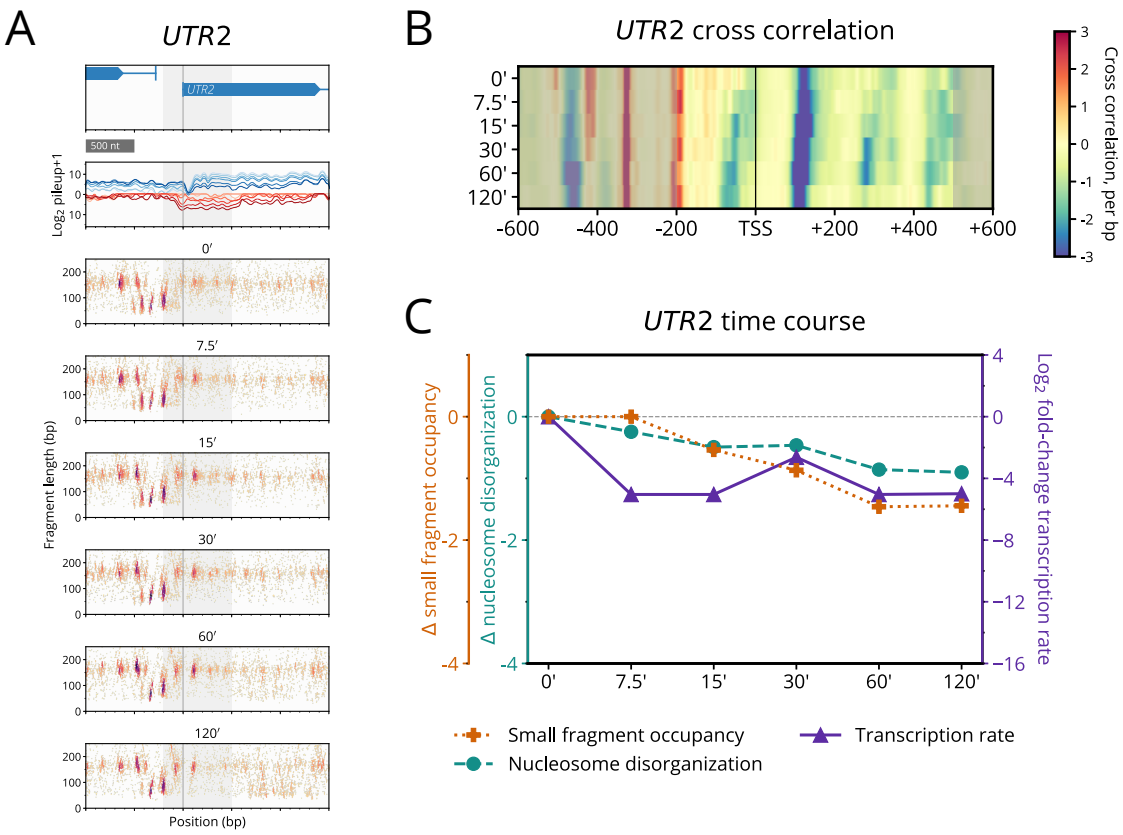

Supplemental Figure S10. *UTR2*, whose overexpression has been linked to endoplasmic reticulum stress (Miller *et al.* 2010), exhibits decreased sense transcription with increased antisense transcription. **(A)** Typhoon plot of *UTR2* shows an inverse change in transcript level on the sense and antisense strands near the 5' end of the ORF of *UTR2*. As *UTR2* is being down-regulated, an antisense transcript is becoming highly expressed. **(B)** Cross-correlation heatmap shows an organization of the +1 nucleosome of *UTR2* as well as an upstream shift of its +1 and +2 nucleosomes (though this would a downstream shift relative to the antisense transcript). **(C)** Line plot of the time course of *UTR2* depicts decreasing chromatin dynamic scores alongside decreased rates of sense transcription.

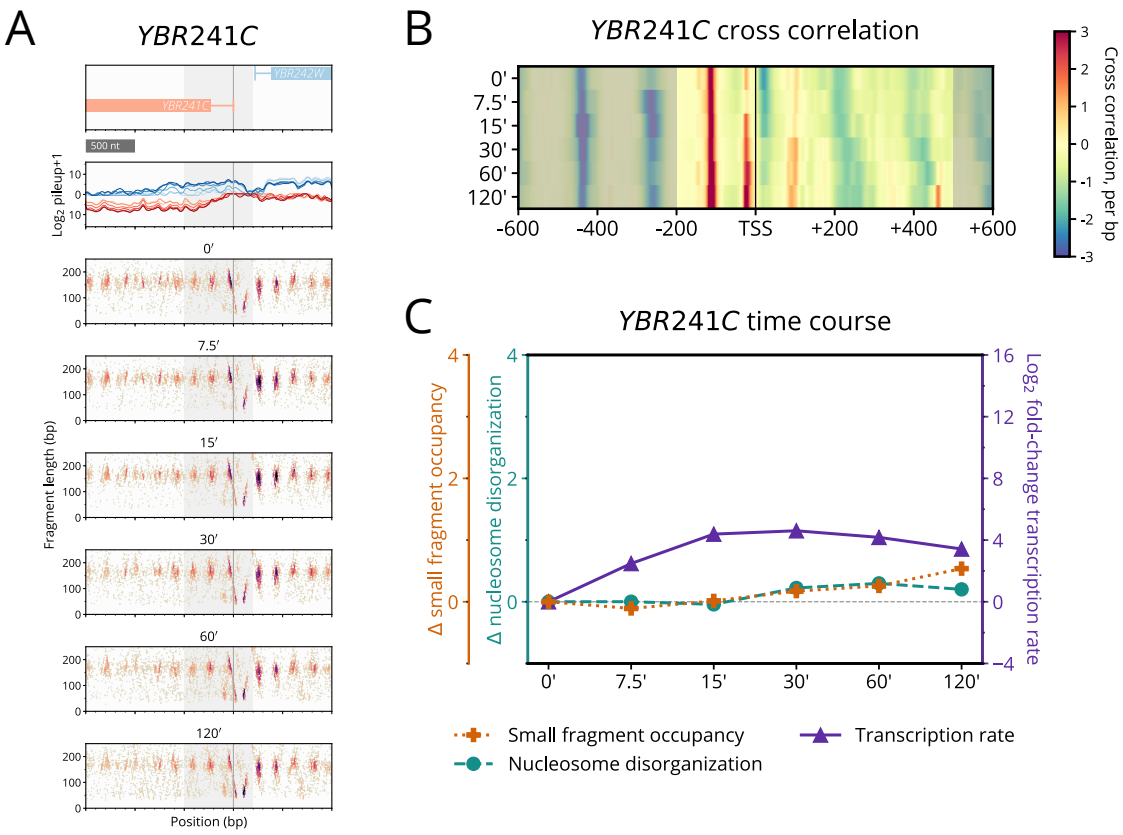

Supplemental Figure S11. *YBR241C*, a gene coding for a vacuole localization protein (Wiederhold *et al.* 2009), exhibits simultaneous activation of both sense and antisense transcription. **(A)** Typhoon plot of *YBR241C* shows activation of both sense transcription and antisense transcripts near the 5' transcript boundary of *YBR241C*. **(B)** Cross-correlation heatmap of chromatin local to its TSS. Gene body nucleosomes disorganize beginning at 30 min and a small factor appears to bind between the +1 and +2 nucleosomes. **(C)** Line plot of the change in chromatin and sense transcription of *YBR241C* through the time course. Its chromatin measures change more subtly than its increased sense transcription, perhaps owing to the effects of increased antisense transcription.

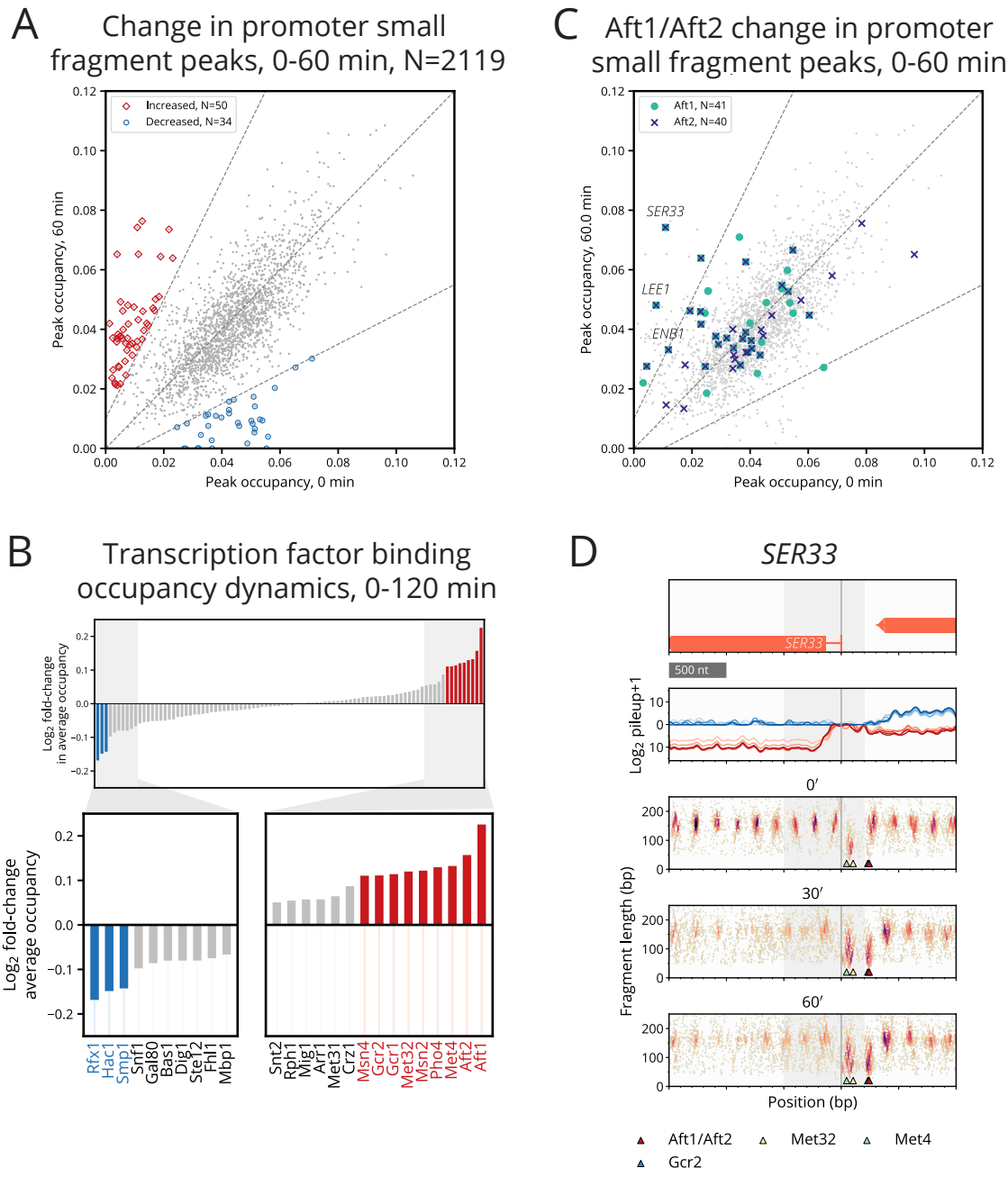

Supplemental Figure S12. Small fragment occupancy in the promoter reveals transcription factor binding dynamics implicated in cadmium stress response. **(A)** Scatter plot of the 0–60 min occupancy change for 2,119 small fragment peaks identified in gene promoters. 50 peaks increased in occupancy by at least double (red), while 34 peaks decreased by at least half (blue). **(B)** Average change in occupancy for promoter peaks per FIMO-assigned TF. TFs are labeled as increased/decreased (red/blue) if the absolute value of their average log-fold change exceeds 0.1. TFs with the greatest increase in binding occupancy include the iron homeostasis regulators Aft1/Aft2, sulfur pathway regulators Met4/Met32, glycolytic activators Gcr1/Gcr2, and general stress

responders Msn2/Msn4. **(C)** Scatter plot of occupancy of Aft1 (turquoise circle) and Aft2 (blue X) at 0 min and 60 min. Aft1 and Aft2 exhibit genome-wide enrichment in binding at 60 min compared to 0 min, particularly in the promoters of a few genes like *SER33*. **(D)** Typhoon plot of *SER33* shows small fragment enrichment at Aft1/Aft2 (red triangle) and Gcr2 (blue triangle, mostly obscured by red triangle) motifs as well as near Met32 (yellow triangle) and Met4 (green triangle) motifs.

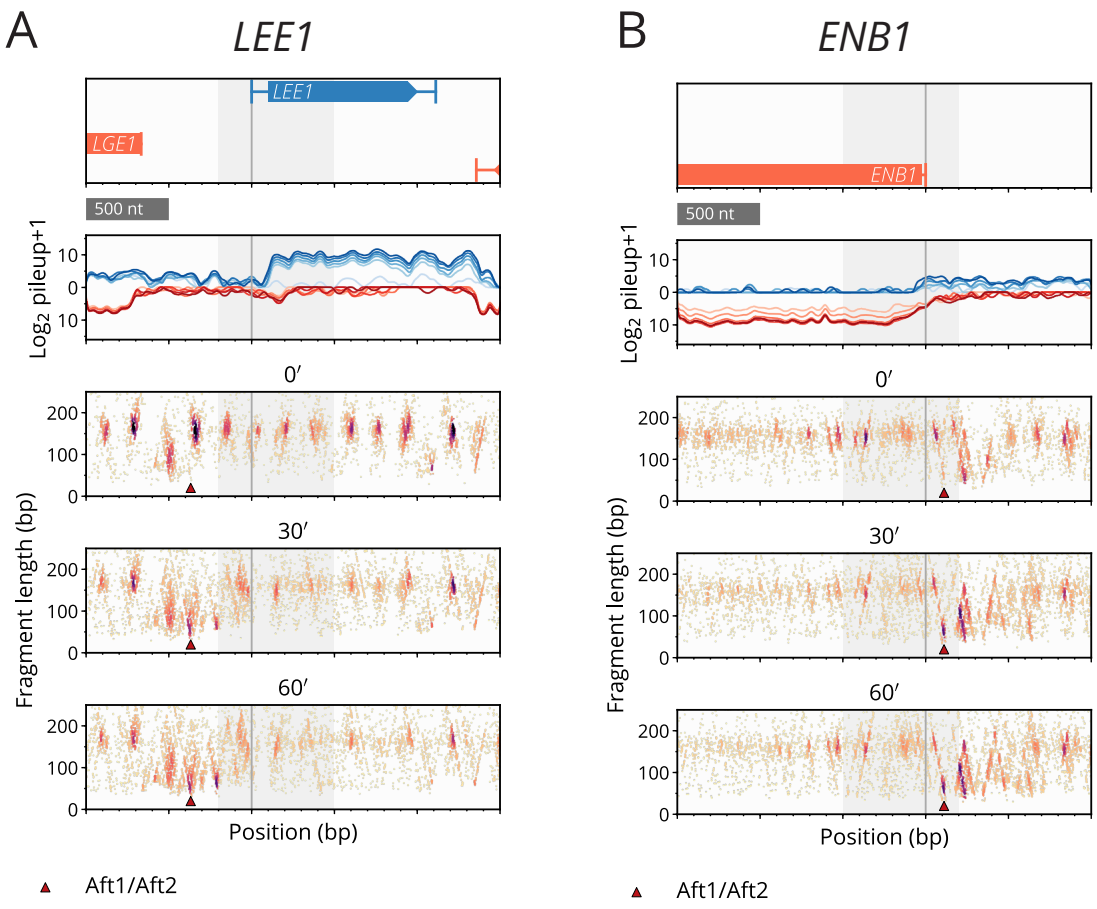

Supplemental Figure S13. Genes with evidence of marked Aft1/Aft2 binding dynamics. **(A)** Gene *LEE1*, coding for an unknown zinc-finger protein, activates with a highly enriched signal of small factor binding at an Aft1/Aft2 binding motif. **(B)** Gene *ENB1*, coding for a ferric enterobactin transmembrane transporter (Heymann *et al.* 2000), activates concurrently with a small fragment enrichment at an Aft1/Aft2 binding motif. Biochemical assays have previously identified Aft1 as a regulator for *ENB1* (Emerson *et al.* 2002).

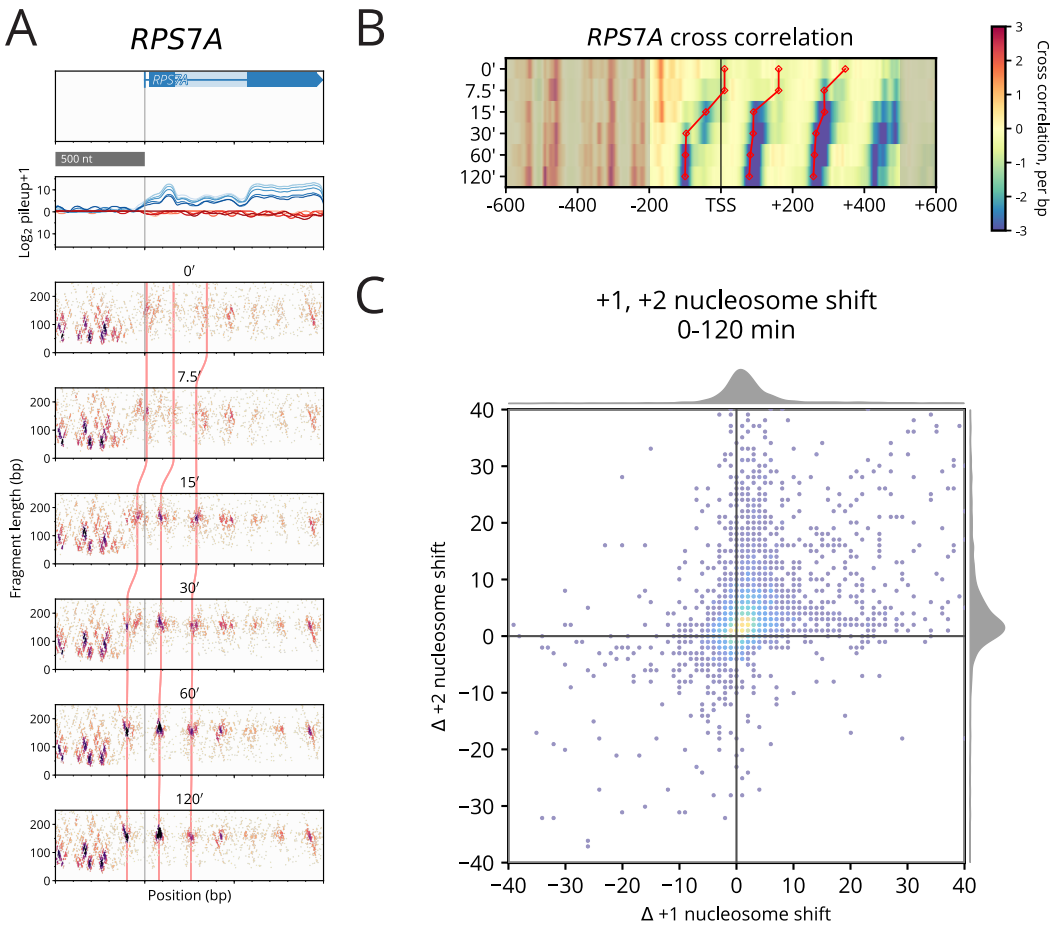

Supplemental Figure S14. Precise determination of +1, +2, and +3 nucleosome positions allows for the characterization of positional changes associated with transcription. **(A)** Annotated typhoon plot of the +1, +2, and +3 nucleosomes of *RPS7A* (red lines indicate center positions over time). Nucleosomes shift upstream concomitantly with the reduction in transcription of *RPS7A*. **(B)** Heatmap of the cross-correlation of the nucleosomes and small factors local to *RPS7A* annotated with called +1, +2, and +3 nucleosome positions (red lines). Peak calling of cross-correlation values allows for tracking of positional movement of nucleosomes across time points. **(C)** Scatter plot of the cumulative positional shift of +1 and +2 nucleosomes through the 120 min time course, for all genes where the positions of those two nucleosomes could be called. A majority of these genes exhibit some downstream shift in both their +1 and +2 nucleosomes (upper right quadrant).

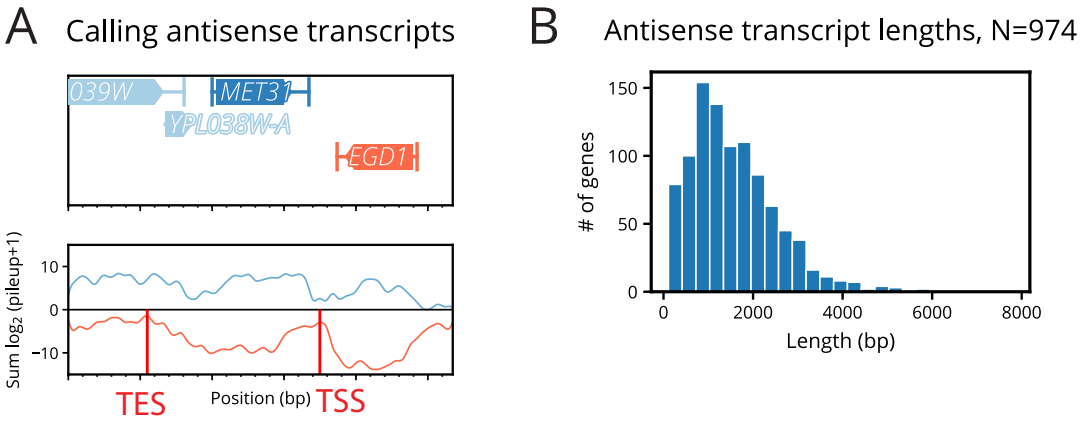

Supplemental Figure S15. Transcript boundaries are called for genes exhibiting significant transcription on their antisense strand. **(A)** Depiction of transcript boundary calling using *MET31* as an example. We call boundaries using the sum of the RNA-seq pileup across the entire time course; adding up the signal over time helps to reduce noise and offers a better chance of identifying valid antisense transcript boundaries. **(B)** Histogram of the length of called antisense transcripts. We found 667 genes that contained antisense transcripts, most of which were between 500–3000 bp long.

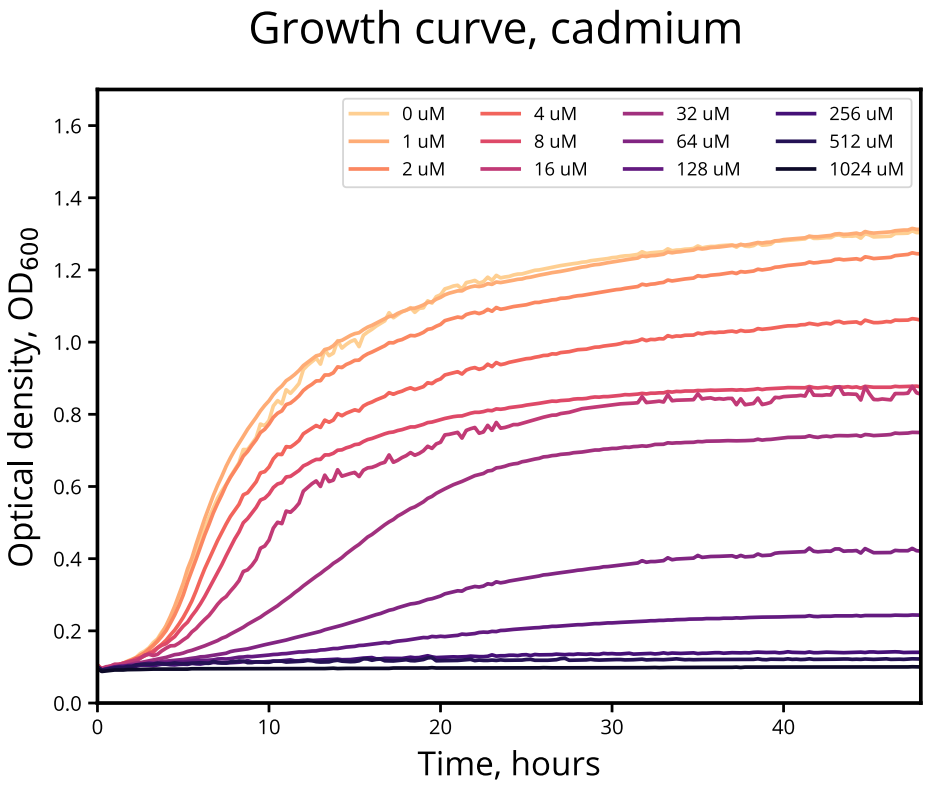

Supplemental Figure S16. OD readings taken every 15 minutes for 48 hours when yeast cells are grown at cadmium concentrations of 0, 1, 2, 4, 8, 16, 32, 64, 128, 258, 512, and 1024 μM. Each concentration was performed in replicate and OD readings were averaged. To study the cell's acute response to cadmium, we ultimately chose to use a concentration of 1000 μM (1 mM), where cells showed no evidence of growth.

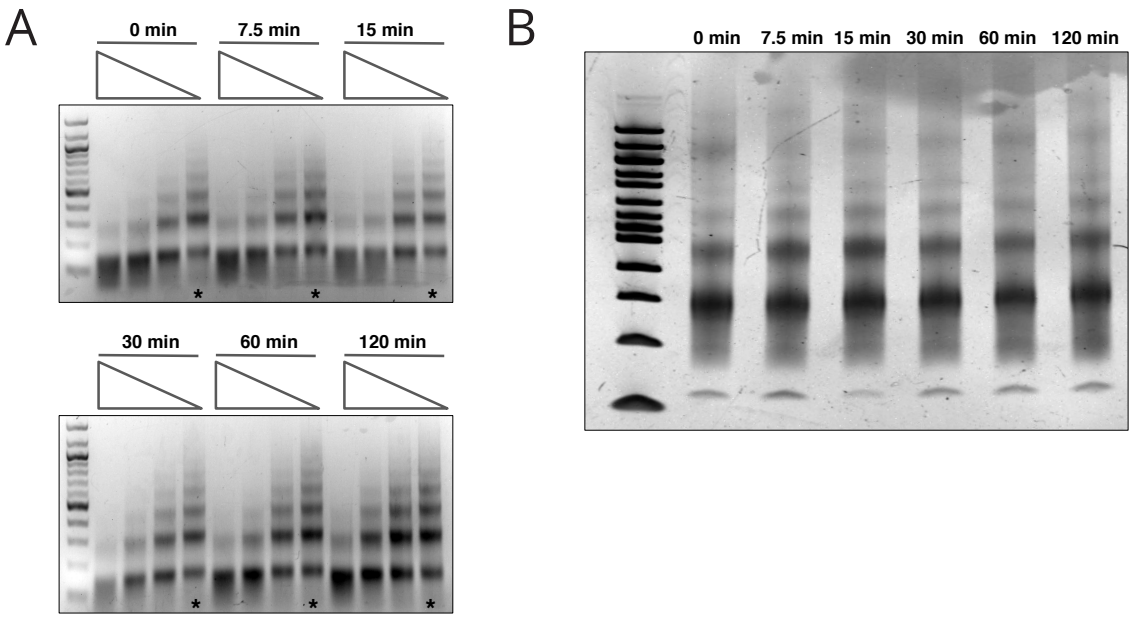

Supplemental Figure S17. Gels to monitor and assess micrococcal nuclease (MNase) digestion. Gels shown here are for replicate 1; gels for replicate 2 show similar levels of consistency across the time course. **(A)** At each time point (0, 7.5, 15, 30, 60, 120 minutes), chromatin extracts were digested with a titration of four MNase concentrations, and the resulting fragments were run in four lanes of a gel (from left to right within each time point: 30, 15, 7.5, 3.75 units of MNase). At each time point, an asterisk indicates the sample ultimately selected for library preparation (in this case, consistently 3.75 units of MNase). **(B)** Using the selected concentration of MNase at each time point, libraries of MNase-digested DNA were run out on a gel to ensure qualitative consistency in the fragment length distributions across the full time course before sending the DNA out for sequencing. Quantitative assessments of the distribution of fragment lengths *after* sequencing are provided in Supplemental Figure S19.

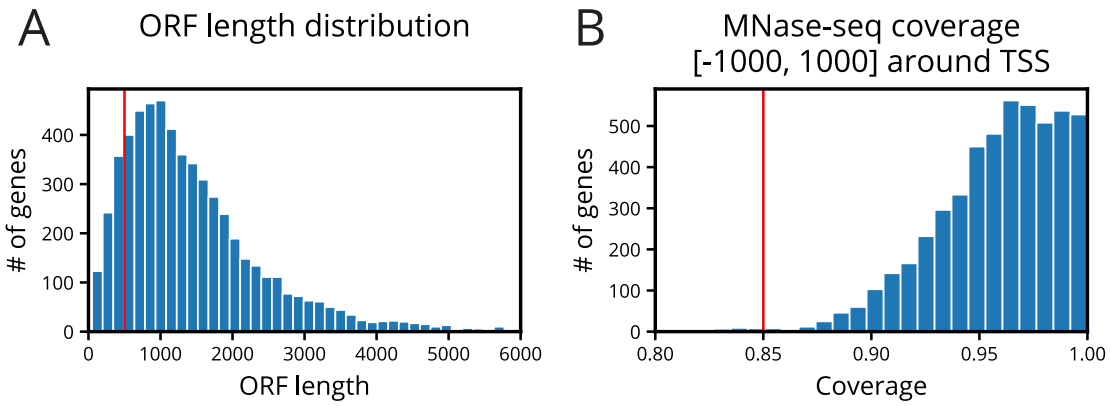

Supplemental Figure S18. Genes selected for analysis must satisfy certain criteria related to minimum ORF length and MNase-seq coverage **(A)** Distribution of ORF lengths. Genes with ORFs shorter than 500 bp (red line) were removed from further analysis. **(B)** Distribution of MNase-seq coverage within 2000 bp window around gene TSSs. Genes with fewer than 85% (red line) covered positions were removed from further analysis.

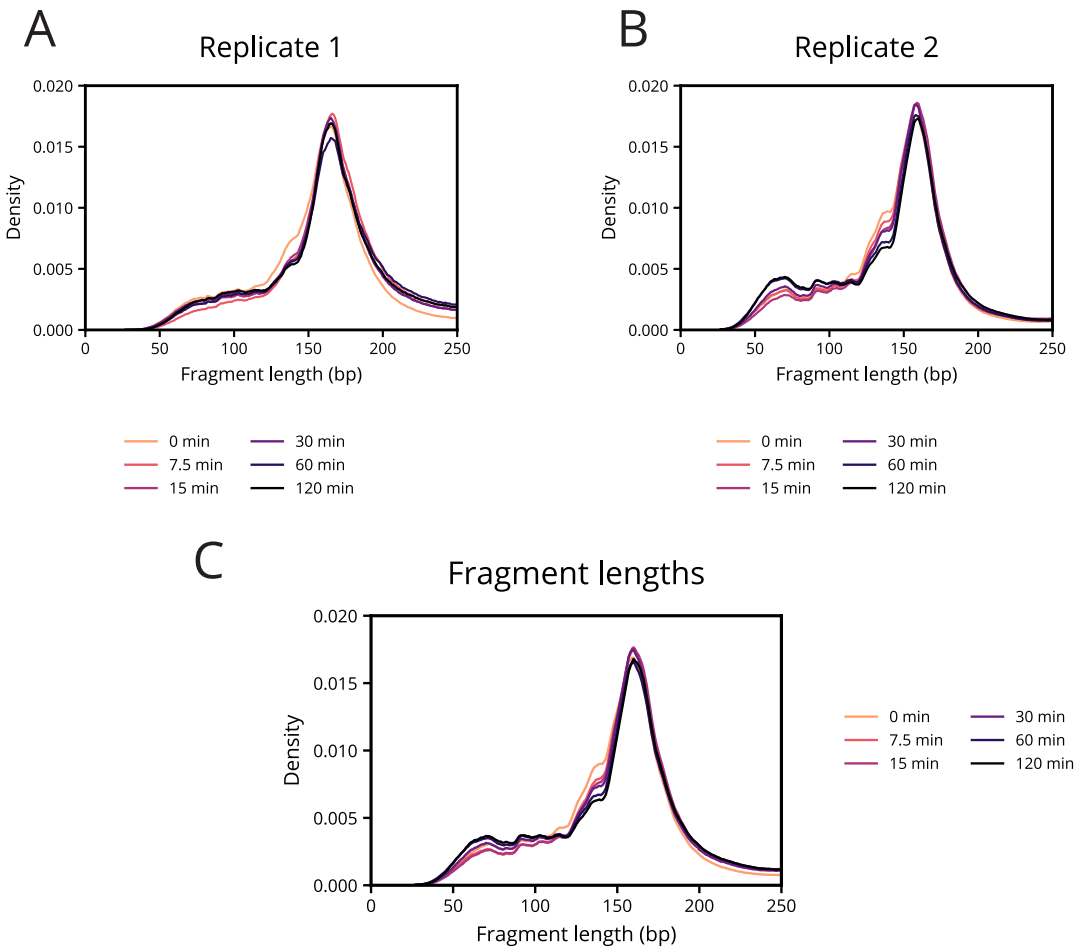

Supplemental Figure S19. Fragment length distributions for the first **(A)** and second **(B)** MNase replicates. The distributions of fragment lengths, for both nucleosomal lengths and shorter lengths, remain quite consistent across all time points in each replicate. **(C)** The fragment length distribution after subsampling and merging the two MNase replicates. In the merged data set, nucleosome-length fragments peak at 159±1 bp at all time points.

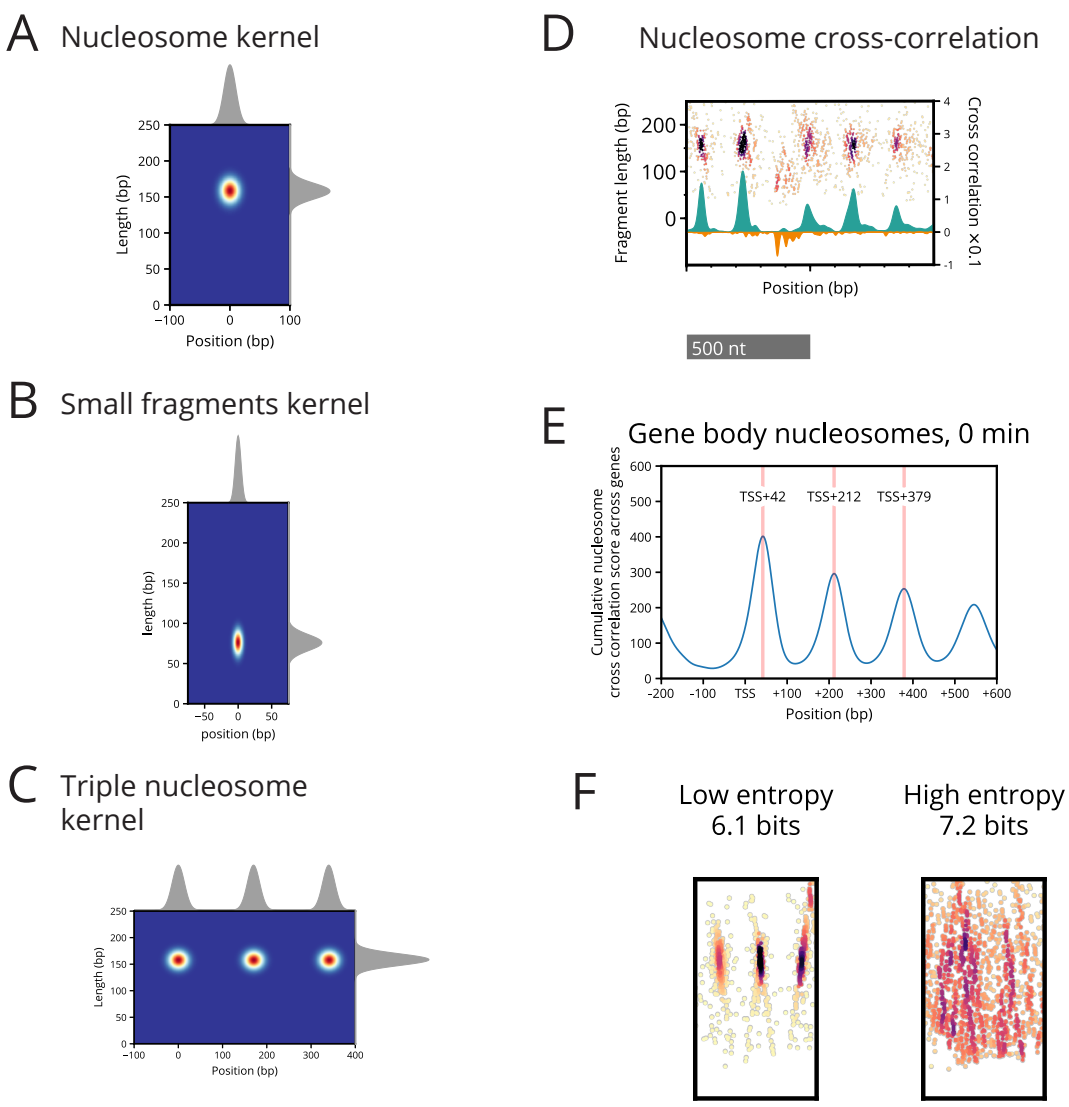

Supplemental Figure S20. Cross-correlation and entropy can be used to characterize the organizational structure of nucleosomes. **(A)** Heatmap of the nucleosome kernel computed using 2,500 well-positioned nucleosomes from Brogaard *et al.* (2012). Well-positioned nucleosome fragments are primarily between 150–170 bp in length. **(B)** Heatmap of the small factor kernel, computed using 151 Abf1 sites from MacIsaac *et al.* (2006). The kernel focuses on fragments 60–90 bp long. **(C)** Heatmap of triple nucleosome kernel, computed to quantify gene body nucleosome organization. **(D)** Typhoon plot exhibits higher values of cross-correlation at positions where MNase-seq fragments best match with nucleosome kernel (turquoise) or small factor kernel (orange). **(E)** Sum of the nucleosome cross-correlation scores at each gene's TSS shows the relative spacing between +1, +2, and +3 nucleosomes. **(F)** Example typhoon plots with low and high entropy values. Low entropy is observed with well-positioned nucleosomes. High entropy is observed when fragments are dispersed with little structure.

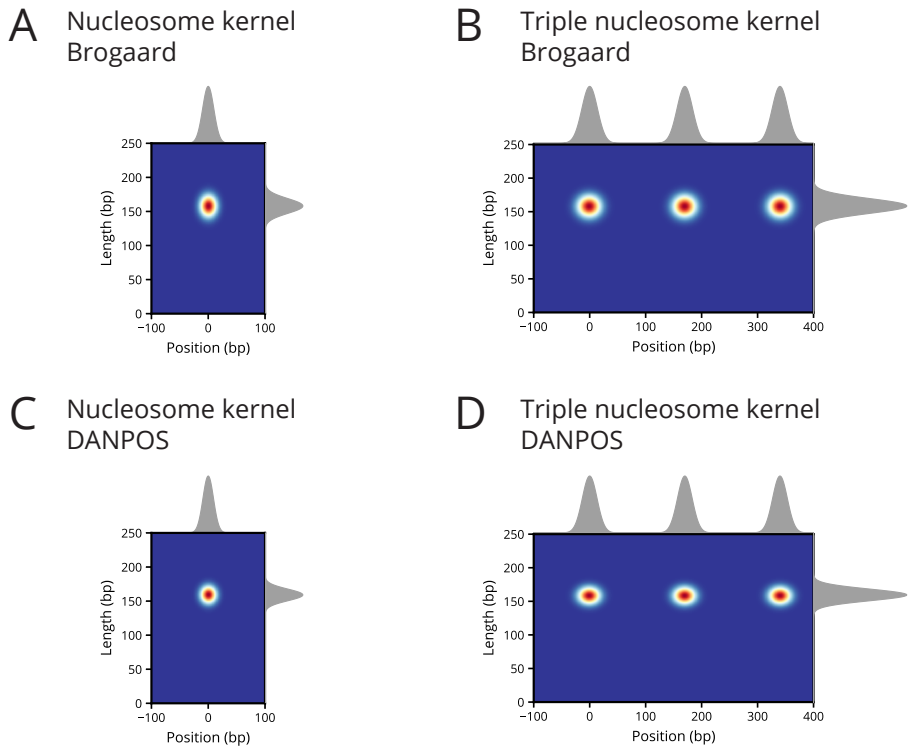

Supplemental Figure S21. Comparison of the nucleosome kernels that arise when using canonical nucleosome positions as reported by Brogaard vs. those called by DANPOS software. **(A, B)** Nucleosome kernels using the 2,500 highest-scoring nucleosome positions as determined by Brogaard and colleagues. **(C, D)** Nucleosome kernels using the 2,500 most-enriched nucleosome positions as called by DANPOS applied to our data. Kernels created from DANPOS sites are comparable to those created from Brogaard sites. DANPOS kernels have a slightly lower variance in their fragment length distribution than Brogaard kernels (8.5 vs. 10.8 bp), likely because the DANPOS sites were derived from our own data, rather than being independent of our data.

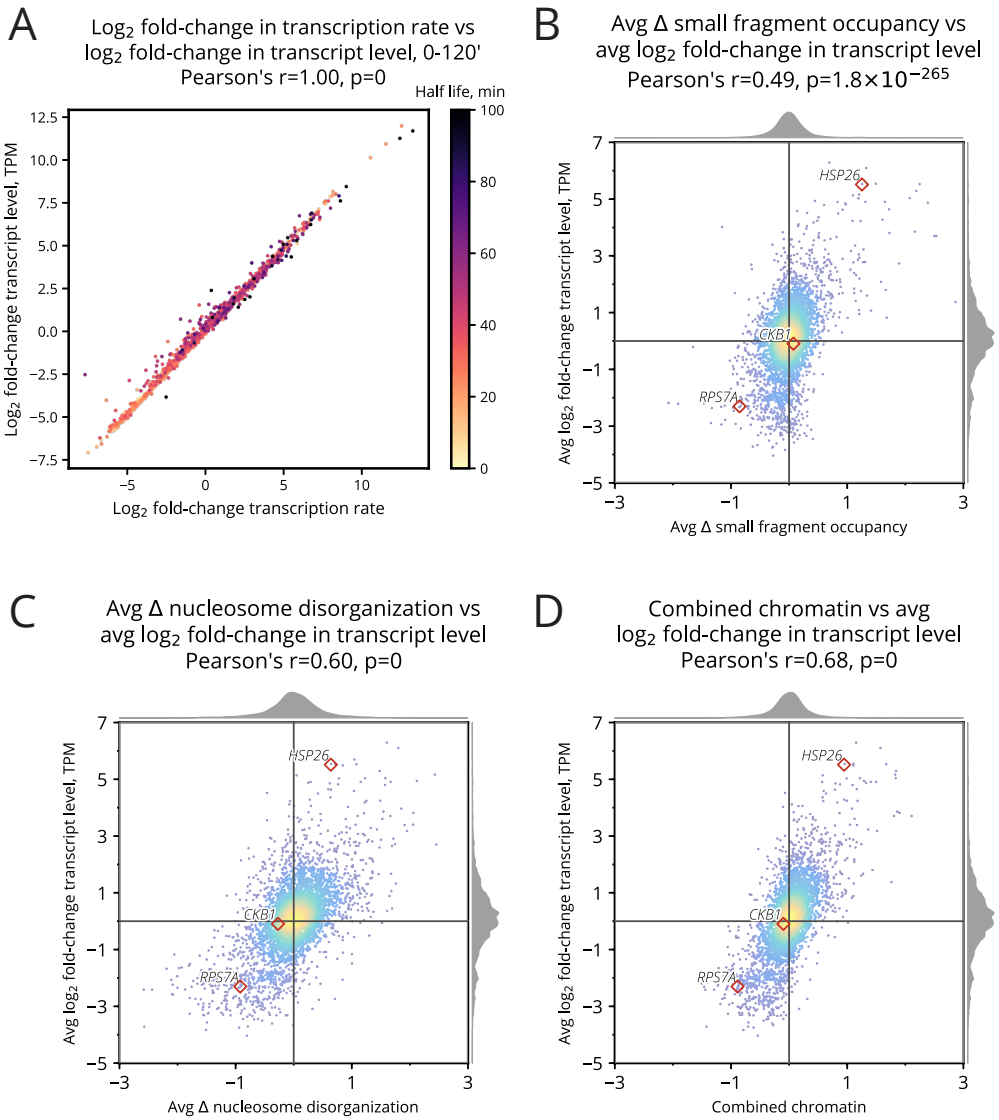

Supplemental Figure S22. Comparison between using $\log_2$ fold-change in transcript level vs. $\log_2$ fold-change in transcription rate when correlating against changes in different chromatin occupancy measures. **(A)** Scatter plot of $\log_2$ fold-change in estimated transcription rate vs. $\log_2$ fold-change in measured transcript level. Coloring indicates the mRNA stability as half life, in minutes. $\log_2$ fold-change in transcription rate is nearly perfectly correlated with $\log_2$ fold-change in transcript level (r=1.00, rounded). **(B–D)** Each of average change in small fragment occupancy, average change in nucleosome disorganization, and combined chromatin score has a correlation with average $\log_2$ fold-change in transcript level that is comparable to its correlation with average $\log_2$ fold-change in transcription rate (compare with Figures 3C, 3D, and S3A, respectively).

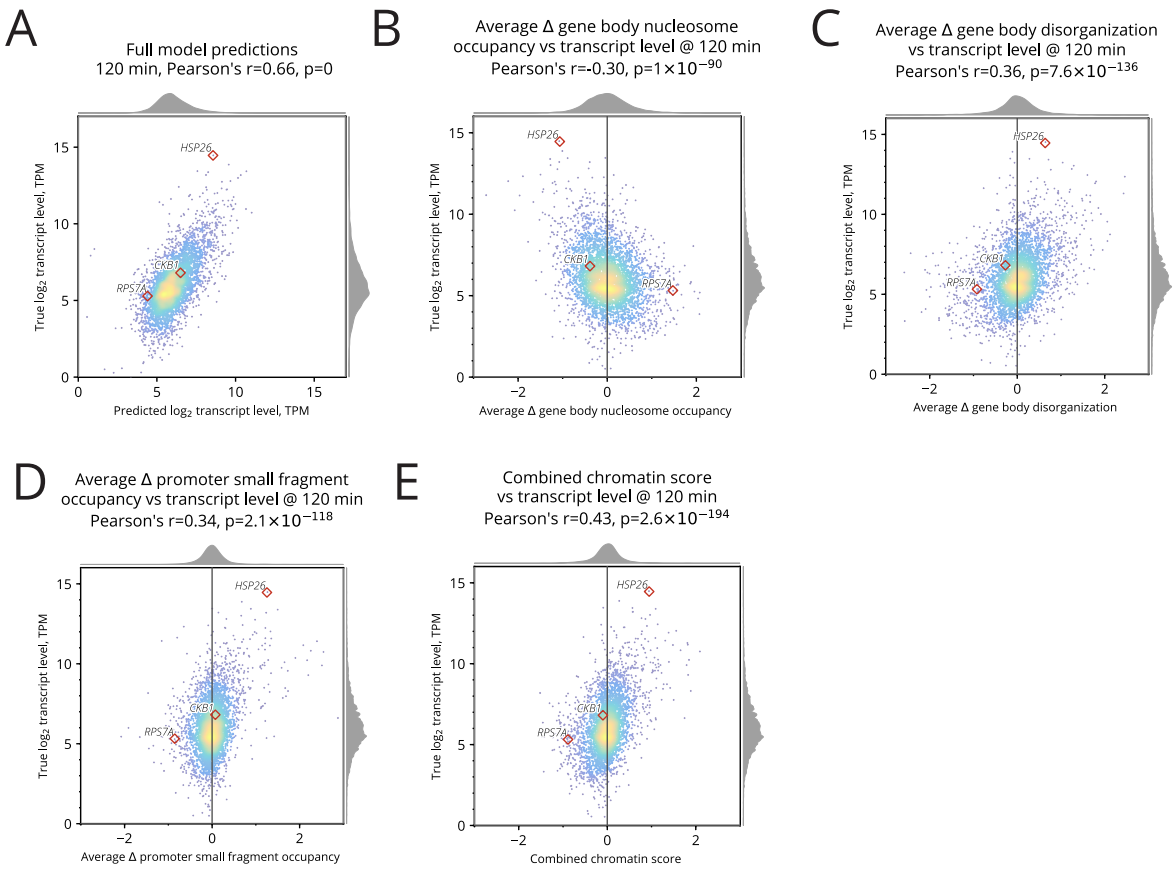

Supplemental Figure S23. Comparison of Gaussian process regression predictions to simpler measures of chromatin changes. **(A)** The predictions of our full regression model after 120 minutes have a Pearson's correlation of 0.67. **(B–E)** In comparison with our full regression model, each of average change in gene body nucleosome occupancy, average change in gene body nucleosome disorganization, average change in promoter small fragment occupancy, and combined chromatin score predict transcript levels with a markedly lower absolute value of correlation, in all cases 0.43 or less. Our combined chromatin score outperforms each of the simpler chromatin measures, but still falls quite short of the full Gaussian process regression model.

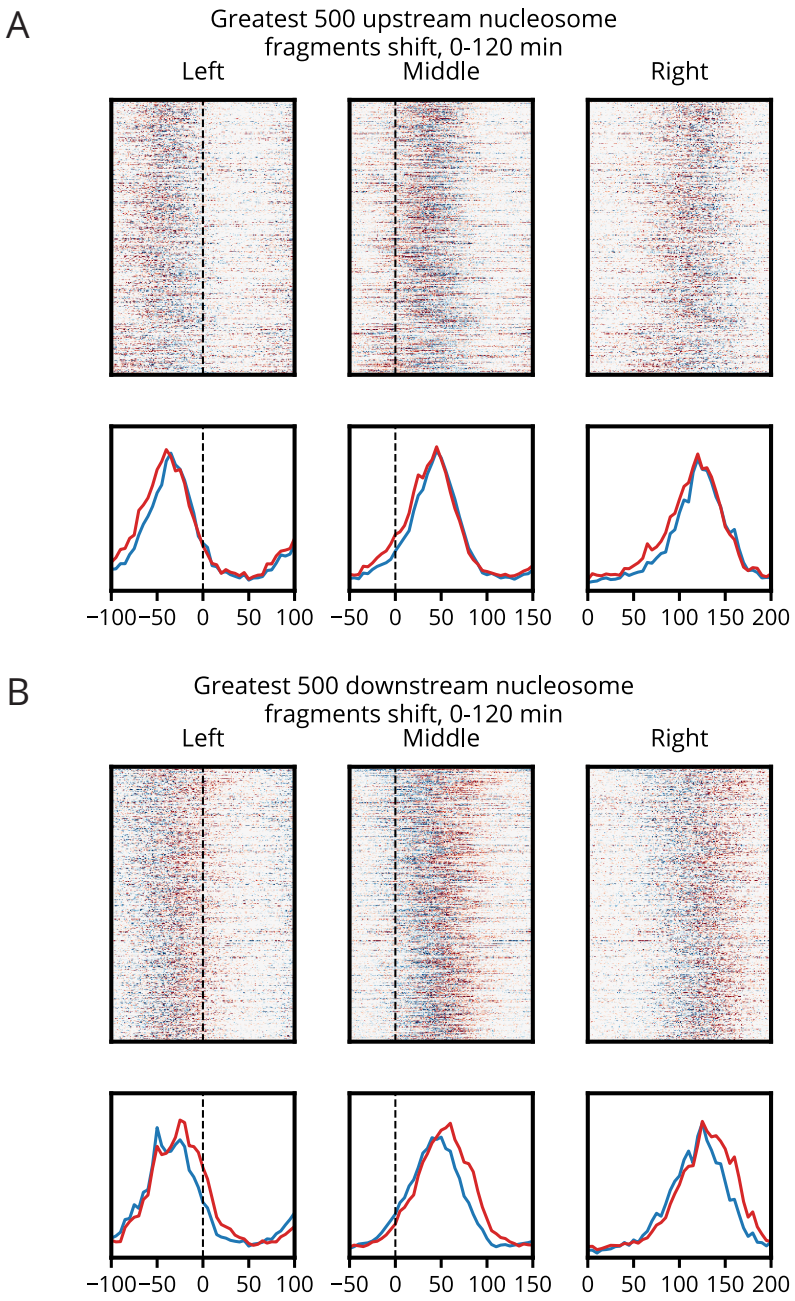

Supplemental Figure S24. MNase fragments local to called +1 nucleosome shifts. **(A)** Genes whose +1 nucleosome shifts upstream the most when analyzed using the middle of MNase fragments, show the same upstream shift when analyzed using left or right ends of fragments. **(B)** Genes whose +1 nucleosome shifts downstream the most when analyzed using the middle of MNase fragments, show the same downstream shift when analyzed using left or right ends of fragments.

GO term	Small Occ.	Nuc. Dis.	Combined	RNA
Translation	22.0	64.9	88.0	88.0
Structural constituent of ribosome	19.2	53.6	76.3	79.4
Cytosolic large ribosomal subunit	15.2	38.5	55.3	63.1
90S preribosome	-	24.8	19.7	48.1
Cytosolic small ribosomal subunit	8.0	27.4	35.8	39.8
Maturation of SSU-rRNA from tricistronic rRNA transcript (SSU-rRNA, 5.8S rRNA, LSU-rRNA)	-	21.8	17.8	32.5
Small-subunit processome	-	15.7	9.6	31.2
rRNA processing	-	7.9	-	24.7
Preribosome, large subunit precursor	-	9.9	-	21.9
Endonucleolytic cleavage in ITS1 to separate SSU-rRNA from 5.8S rRNA and LSU-rRNA from tricistronic rRNA transcript (SSU-rRNA, 5.8S rRNA, LSU-rRNA)	-	6.5	-	21.8
Ribosomal large subunit biogenesis	-	6.1	-	20.2
Ribosomal large subunit assembly	-	-	-	15.6
Endonucleolytic cleavage to generate mature 5'-end of SSU-rRNA from (SSU-rRNA, 5.8S rRNA, LSU-rRNA)	-	-	-	15.0
Endonucleolytic cleavage in 5'-ETS of tricistronic rRNA transcript (SSU-rRNA, 5.8S rRNA, LSU-rRNA)	-	-	-	14.5
snoRNA binding	-	6.0	-	13.0
Ribosomal small subunit assembly	-	6.9	8.5	7.1
Maturation of LSU-rRNA from tricistronic rRNA transcript (SSU-rRNA, 5.8S rRNA, LSU-rRNA)	-	-	-	7.7
t-UTP complex	-	-	-	6.0
RNA binding	-	-	5.9	5.6
Maturation of 5.8S rRNA from tricistronic rRNA transcript (SSU-rRNA, 5.8S rRNA, LSU-rRNA)	-	-	-	5.2

Supplemental Table S1. Gene Ontology (GO) terms for genes with the greatest organization in chromatin or decrease in transcript level. Score is the $-\log_{10}$ FDR of the term. Most of the highest scoring GO terms identified by RNA, relating to translation, are also identified by GO using changes in the chromatin.

GO term	Small Occ.	Nuc. Dis.	Combined	RNA
Sulfate assimilation	3.9	1.4	3.8	5.8
Alditol:NADP+ 1-oxidoreductase activity	0.9	-	1.0	3.9
Response to stress	3.9	-	1.8	3.3
Autophagy of mitochondrion	-	-	-	2.7
Cellular response to oxidative stress	-	-	-	2.6
Sulfur amino acid metabolic process	-	1.3	2.6	-
Arabinose catabolic process	-	-	-	2.2
D-xylose catabolic process	-	-	-	2.2
Protein localization by the Cvt pathway	-	-	-	2.2
Phagophore assembly site	-	-	-	2.2
Protein refolding	-	2.1	1.5	-
Methionine metabolic process	0.8	1.6	1.7	-
Methionine biosynthetic process	1.2	-	1.4	1.6
Fungal-type vacuole lumen	1.5	-	0.8	1.0
Negative regulation of gluconeogenesis	-	-	-	1.5
Unfolded protein binding	0.9	-	1.5	0.7
Glycolytic process	1.4	-	-	1.1
Protein quality control for misfolded or incompletely synthesized proteins	-	1.4	-	-
Aldo-keto reductase (NADP) activity	-	-	-	1.2
Glutathione transferase activity	-	-	-	1.2
Transmembrane transport	-	-	-	1.2
Protein catabolic process in the vacuole	-	-	-	1.1
Structural constituent of ribosome	-	-	1.0	-
GID complex	-	-	-	1.0

Supplemental Table S2. Gene Ontology (GO) terms for genes with the greatest disorganization in chromatin or increase in transcript level. Score is the $-\log_{10}$ FDR of the term. Many of the highest scoring GO terms identified by RNA, such as those relating to sulfur assimilation, stress, and protein folding, are also identified by GO using changes in the chromatin, although some relating to sugar metabolism are identified by RNA but not by chromatin measures.

Supplemental Method S1. Preparing MNase and RNA sequencing libraries and aligning reads to the genome

Preparing MNase sequencing libraries
Illumina sequencing libraries of MNase-treated DNA were prepared using 500 ng of DNA as previously described (Henikoff *et al.* 2011).

Preparing RNA sequencing libraries
Illumina sequencing libraries of total RNA were prepared using the Illumina TruSeq Stranded Total RNA Human/Mouse/Rat kit (Cat number RS-122-2201) following the protocol provided by Illumina with Ribo-Zero.

Aligning sequencing reads to the genome
All reads were aligned to the sacCer3/R64 version of the *S. cerevisiae* genome using Bowtie 0.12.7 (Langmead *et al.* 2009).

The recovered sequences from all paired-end MNase reads were truncated to 20 bp and aligned in paired-end mode using the following Bowtie parameters: `--wrapper basic-0 --time -p 32 -n 2 -l 20 --phred33-quals -m 1 --best --strata -S`.

The recovered sequences from all single-end RNA reads were truncated to 51 bp and aligned in single-end mode using the same Bowtie parameters.

Supplemental Method S2. Analyzing Gene Ontology enrichment

GO enrichment analysis was performed using GOATOOLS (Klopfenstein *et al.* 2018) with the go-basic.obo annotations from the Gene Ontology Consortium (Ashburner *et al.* 2000; The Gene Ontology Consortium 2019). False discovery rate was corrected using the Benjamini-Hochberg procedure (Benjamini and Hochberg 1995).

Supplemental Method S3. Clustering genes based on chromatin measures

Genes with the greatest increase in average small fragment occupancy or average nucleosome disorganization were chosen for clustering. The top 500 genes for each measure were combined into a final set of 832 (fewer than 1000 because many genes were in both sets).

Clustering was performed in SciPy (Virtanen *et al.* 2020) using hierarchical clustering on the basis of pair-wise Euclidean distance between z-normalized measures of change in small fragment occupancy and nucleosome disorganization. Ward linkage was chosen for its efficient approximation to the minimal sum of squares objective (Ward 1963). Eight clusters were ultimately chosen to balance the interpretability of fewer clusters with the significance of identified GO terms in smaller and more homogeneous but more numerous clusters.

Supplemental Method S4. Calling +1, +2, +3 nucleosomes and linking them over time

Nucleosomes were called using peaks of the nucleosome cross-correlation scores local to each gene's TSS. Peaks within a 1000 bp window around the TSS were sorted by score. The position with the greatest peak score was labeled as a nucleosome center and removed. Positions within 80 bp were also removed. This procedure was repeated until all peak positions were removed and nucleosomes called for this 1000 bp window.

"Linked" nucleosomes are defined as nucleosomes across the time course that nominally represent the same underlying nucleosome even though its position may have shifted or become more or less fuzzy. Nucleosomes were linked across time points using a nearest-neighbor approach. In a greedy manner, the most well-positioned nucleosome (lowest disorganization score) was considered first. The position of this nucleosome was used to identify the linked nucleosomes in previous and subsequent time points by considering the nearest nucleosome in each of the respective time points within 100 bp of the original nucleosome's position.

Each gene's +1 nucleosome was called by identifying the linked nucleosome closest to the TSS. The +2 and +3 nucleosomes were computed as the next nucleosomes at least 80 bp downstream from the preceding one.

While nucleosome positions were computed using fragment centers, these positions were not affected by overdigestion of either fragment end by MNase (Supplemental Fig. S24A, B).

Supplemental Method S5. Merging replicate MNase and RNA samples

MNase and RNA replicates were confirmed to have a high concordance through parallel analyses of each replicate including GO enrichment analyses (Supplemental Fig. S4A, B, C, D). After this confirmation, replicates were merged using the following procedure.

Replicates A and B are defined as sets of reads from six samples across the time course, while T is the set of times at which those samples were taken:

$$A = \{a_0, a_{7.5}, a_{15}, a_{30}, a_{60}, a_{120}\}$$
$$B = \{b_0, b_{7.5}, b_{15}, b_{30}, b_{60}, b_{120}\}$$
$$T = \{0, 7.5, 15, 30, 60, 120\}$$

Separately for each replicate, the time point with the fewest reads determined that replicate's subsampling depth (k_A and k_B):

$$k_A = \min_{t \in T} |a_t| \ , \ k_B = \min_{t \in T} |b_t|$$

The reads at each time point in each replicate were then subsampled (uniformly at random) to that replicate's subsampling depth in order to form new sets A' and B':

$$A' = \{a'_0, \ldots, a'_{120}\}$$
$$B' = \{b'_0, \ldots, b'_{120}\}$$
$$|a'_t| = k_A \ , \ |b'_t| = k_B \ , \ \forall t \in T$$

Finally, the sets of subsampled reads were merged into a superset, M, for downstream analysis:

$$M = \{m_0, \ldots, m_{120}\} = \{a'_0 \cup b'_0, \ldots, a'_{120} \cup b'_{120}\}$$

This procedure yields the highest possible overall read depth for the merged superset while still maintaining a consistent depth and a consistent proportion of reads between replicates A and B across all of the time points.

Supplemental Method S6. Details for gene set selection

Genes whose ORFs are less than 500 bp (Supplemental Fig. S18A) long were omitted in order to ensure valid "gene body" calculations between [TSS, +500]. TSS annotations were determined by Park *et al.* (2014). For five genes, *SUL1*, *SUL2*, *MET32*, *HSP26*, and *BDS1*, we manually annotated the TSS to be consistent with the RNA-seq data in this study. We required a half-life for each gene in order to estimate transcription rates. MNase-seq coverage was computed in a 2,000 bp window centered on each gene's TSS. A position in this window is considered "covered" when there exists at least one fragment whose center is at this position. MNase coverage was then defined as the number of covered positions in this window divided by the length of the window, 2,000 bp. Genes with MNase coverage below 0.85 (n=109) were excluded from further analysis (Supplemental Fig. S18B).

Supplemental Method S7. Estimating transcription rates

Transcription rates were computed for each gene using a zero-order growth with first-order decay relationship:

$$\begin{aligned}\frac{dC_i}{dt} &= R_i - k \cdot C_i \\ C_i &= \frac{R_i}{k} + G_i \cdot e^{-kt_i} \\ t_i &\in \{7.5, 15, 30, 60, 120\}, \text{ s.t. } i \in \{1, \ldots, 5\}\end{aligned}$$

where C_i is the gene's total RNA concentration measured by RNA-seq for sample i, k is its (fixed) decay rate, G_i is the concentration of its RNA governed by zero-order growth, and R_i is its unknown transcription rate. Assuming a constant rate of transcription between time points, we can solve for R_i and G_i using pairs of difference equations:

$$\begin{aligned}C_{i-1} &= \frac{R_i}{k} + G_i \cdot e^{-k \cdot t_{i-1}} \\ C_i &= \frac{R_i}{k} + G_i \cdot e^{-k \cdot t_i}\end{aligned}$$

Similarly, steady-state transcription rates, R_0 at t_0, were computed by setting the rate of production equal to the rate of decay:

$$\begin{aligned}t_0 = 0, i = 0 \\ R_0 = k \cdot C_0\end{aligned}$$

To compute the decay rate k for a given gene, a half-life value τ was computed as an average of the values reported in three previous studies (Geisberg *et al.* 2014; Miller *et al.* 2011; Presnyak *et al.* 2015). The gene's decay rate was then set to the inverse of the average half-life, $k = 1/\tau$.

Because the above method may compute a transcription rate as being less than or equal to 0 at some time point, rates were floored to be at least 0.1 TPM/min so as to facilitate reasonable evaluations of fold change.

The computed transcription rates significantly correlate with measured mRNA abundance (Supplemental Fig. S22A) and correlate with measures of the chromatin (Fig. 2C, Fig. 2D, Supplemental Fig. S3A) nearly identically to how mRNA abundance correlates with measures of the chromatin (Supplemental Fig. S22B Supplemental Fig. S22C, Supplemental Fig. S22D).

References

Ashburner M, Ball CA, Blake JA, Botstein D, Butler H, Cherry JM, Davis AP, Dolinski K, Dwight SS, Eppig JT, Harris MA, Hill DP, Issel-Tarver L, Kasarskis A, Lewis S, Matese JC, Richardson JE, Ringwald M, Rubin GM, Sherlock G. 2000. Gene Ontology: Tool for the unification of biology. *Nat. Genet.* **25**: 25–29.

Benjamini Y, Hochberg Y. 1995. Controlling the false discovery rate: A practical and powerful approach to multiple testing. *J. R. Stat. Soc. Series B Stat. Methodol.* **57**: 289–300.

Brogaard K, Xi L, Wang JP, Widom J. 2012. A map of nucleosome positions in yeast at base-pair resolution. *Nature* **486**: 496–501.

Emerson LR, Nau ME, Martin RK, Kyle DE, Vahey M, Wirth DF. 2002. Relationship between chloroquine toxicity and iron acquisition in Saccharomyces cerevisiae. *Antimicrob. Agents Chemother.* **46**: 787–796.

Geisberg JV, Moqtaderi Z, Fan X, Ozsolak F, Struhl K. 2014. Global analysis of mRNA isoform half-lives reveals stabilizing and destabilizing elements in yeast. *Cell* **156**: 812–824.

Henikoff JG, Belsky JA, Krassovsky K, MacAlpine DM, Henikoff S. 2011. Epigenome characterization at single base-pair resolution. *Proc. Natl. Acad. Sci. USA* **108**: 18318–18323.

Heymann P, Ernst JF, Winkelmann G. 2000. A gene of the major facilitator superfamily encodes a transporter for enterobactin (Enb1p) in Saccharomyces cerevisiae. *Biometals* **13**: 65–72.

Klopfenstein DV, Zhang L, Pedersen BS, Ramírez F, Warwick Vesztrocy A, Naldi A, Mungall CJ, Yunes JM, Botvinnik O, Weigel M, Dampier W, Dessimoz C, Flick P, Tang H. 2018. GOATOOLS: A Python library for Gene Ontology analyses. *Sci. Rep.* **8**: 10872.

Langmead B, Trapnell C, Pop M, Salzberg SL. 2009. Ultrafast and memory-efficient alignment of short DNA sequences to the human genome. *Genome Biol.* **10**: R25.

Lyons TJ, Gasch AP, Gaither LA, Botstein D, Brown PO, Eide DJ. 2000. Genome-wide characterization of the Zap1p zinc-responsive regulon in yeast. *Proc. Natl. Acad. Sci. USA* **97**: 7957–7962.

MacIsaac KD, Wang T, Gordon DB, Gifford DK, Stormo GD, Fraenkel E. 2006. An improved map of conserved regulatory sites for Saccharomyces cerevisiae. *BMC Bioinformatics* **7**: 113.

Miller C, Schwalb B, Maier K, Schulz D, Dümcke S, Zacher B, Mayer A, Sydow J, Marcinowski L, Dölken L, Martin DE, Tresch A, Cramer P. 2011. Dynamic transcriptome

analysis measures rates of mRNA synthesis and decay in yeast. *Mol. Syst. Biol.* **7**: 458.

Miller KA, DiDone L, Krysan DJ. 2010. Extracellular secretion of overexpressed glycosylphosphatidylinositol-linked cell wall protein Utr2/Crh2p as a novel protein quality control mechanism in Saccharomyces cerevisiae. *Eukaryot. Cell* **9**: 1669–1679.

Park D, Morris AR, Battenhouse A, Iyer VR. 2014. Simultaneous mapping of transcript ends at single-nucleotide resolution and identification of widespread promoter-associated non-coding RNA governed by TATA elements. *Nucleic Acids Res.* **42**: 3736–3749.

Presnyak V, Alhusaini N, Chen YH, Martin S, Morris N, Kline N, Olson S, Weinberg D, Baker KE, Graveley BR, Coller J. 2015. Codon optimality is a major determinant of mRNA stability. *Cell* **160**: 1111–1124.

The Gene Ontology Consortium. 2019. The Gene Ontology Resource: 20 years and still GOing strong. *Nucleic Acids Res.* **47**: D330–D338.

Venters BJ, Wachi S, Mavrich TN, Andersen BE, Jena P, Sinnamon AJ, Jain P, Rolleri NS, Jiang C, Hemeryck-Walsh C, Pugh BF. 2011. A comprehensive genomic binding map of gene and chromatin regulatory proteins in Saccharomyces. *Mol. Cell* **41**: 480–492.

Virtanen P, Gommers R, Oliphant TE, Haberland M, Reddy T, Cournapeau D, Burovski E, Peterson P, Weckesser W, Bright J, van der Walt SJ, Brett M, Wilson J, Jarrod Millman K, Mayorov N, Nelson ARJ, Jones E, Kern R, Larson E, Carey C, Polat İ, Feng Y, Moore EW, Vand erPlas J, Laxalde D, Perktold J, Cimrman R, Henriksen I, Quintero EA, Harris CR, Archibald AM, Ribeiro AH, Pedregosa F, van Mulbregt P, Contributors S. 2020. SciPy 1.0: Fundamental algorithms for scientific computing in Python. *Nature Methods* **17**: 261–272.

Ward JH. 1963. Hierarchical grouping to optimize an objective function. *J. Am. Stat. Assoc.* **58**: 236–244.

Wiederhold E, Gandhi T, Permentier HP, Breitling R, Poolman B, Slotboom DJ. 2009. The yeast vacuolar membrane proteome. *Mol. Cell. Proteomics* **8**: 380–392.